Ocean Engineering 324 (2025) 120673

Contents lists available at ScienceDirect

Ocean Engineering

journal homepage: www.elsevier.com/locate/oceaneng

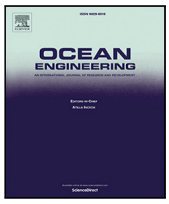

Research paper

The influence of the modeling order on the predictable area of non-linear unidirectional ocean waves

Marco Klein [a,*], Helene Lünser [b], Moritz Hartmann [a], Sören Ehlers [a], Norbert Hoffmann [b,c], Nicolas Desmars [a]

[a] Institute of Maritime Energy Systems, German Aerospace Center (DLR), 21502 Geesthacht, Germany
[b] Dynamics Group, Hamburg University of Technology, 21073 Hamburg, Germany
[c] Department of Mechanical Engineering, Imperial College London, London SW7 2AZ, United Kingdom

ARTICLE INFO

Keywords:
Ocean waves
Deterministic prediction
Predictable area
Non-linear waves

ABSTRACT

The influence of non-linear modeling of phase-resolved ocean wave fields on the extent of the accessible predictable area is investigated. Assuming that the ocean surface dynamics is known over a limited spatial domain, e.g. via radar backscatter reconstruction, the linear wave theory as well as the high-order spectral method with various orders of non-linearity are used to propagate the surface with different levels of physical fidelity. The prediction accuracy is quantified by comparing the predicted waves to a reference, i.e. a fully known wave field propagated with a high-fidelity wave model. By doing this, it is made possible to track the spatiotemporal evolution of the prediction accuracy and define the predictable area as the region over which the accuracy is higher than a threshold, here defined by a "surface similarity parameter" lower than 0.1. Different unidirectional wave field characteristics are studied, highlighting the effect of the wave steepness, water depth and wave energy spreading around the peak spectral frequency, all impacting significantly the prediction accuracy, thus the predictable area. It is shown that the extent of the predictable area is highly dependent on the order of the considered wave model, and that the third order generally leads to the largest reachable predictable area in all configurations.

1. Introduction

For many offshore maneuvers, such as ship crew transfers during the construction and maintenance of marine systems, one criterion for operability is the limiting wave height. To determine future time windows of safe operations, forecasts of sea states' statistical characteristics are used as a basis for estimating the expected maximum wave height. However, such forecasts dismiss the phase information of the wave field, which prevents the prediction of the actual sea surface elevation and leads to over-conservative choices of suitable time windows.

Safer and more efficiently managed offshore operations may be obtained by using deterministic wave predictions, that provide a wave-by-wave description of the surface evolution in the near future. Such predictions rely on the knowledge of the surrounding wave conditions which can be measured from different types of in situ sensors such as wave buoys, ADCPs or pressure transducers, or remote sensors like marine radars or stereovideo cameras. The latter ones have the advantage of being able to follow the trajectory of the structure over which they are mounted (e.g. a moving vessel) and have more direct access to information about the directionality of the measured wave field.

Regardless of how the wave data is measured, an essential prerequisite for a prediction is that the wave simulation method is numerically efficient enough to be real-time capable while ensuring a sufficient level of accuracy of the underlying physics. In this context, real-time capability means that the numerical prediction of the future wave field must provide results substantially earlier than the time of arrival of the physical wave field at the corresponding prediction location. Due to the constraint of real-time capability, the selection of applicable methods is significantly reduced. For this reason, only wave models based on potential theory (irrotational flow, incompressible and inviscid fluid) are currently being considered as applicable methods for deterministic wave prediction. As a consequence, complex nonlinear effects (e.g. wave breaking, short-term wind-wave effects, etc.) are generally omitted in deterministic wave prediction.

A very efficient numerical method is the widely used linear wave theory, also known as Airy theory (Airy, 1845). Based on this method, Payer and Rathje (2004) have presented a system to support ship

* Corresponding author.
E-mail address: marco.klein@dlr.de (M. Klein).

https://doi.org/10.1016/j.oceaneng.2025.120673
Received 8 April 2024; Received in revised form 3 January 2025; Accepted 11 February 2025
Available online 22 February 2025

navigation which is based on continuous X-band radar measurements. Clauss et al. (2007) have used surface elevation snapshots as a basis for linear wave predictions and obtained satisfactory results for moderate unidirectional sea states. This method has been extended by Clauss et al. (2012) and Kosleck (2013) to predict directional sea states and implied ship motions. Naaijen and Huijsmans (2008, 2010) as well as Naaijen et al. (2009, 2014) have used the linear wave theory for real-time wave and ship motion prediction in both unidirectional and directional waves. However, the assumptions behind the linearization of the water wave problem may lead to inaccuracies that become significant for larger wave steepness and longer prediction times, i.e. limiting the range of applicability of the linear wave theory for deterministic wave prediction. At the expense of a higher computational effort, non-linear methods allow for a more accurate representation of the ocean surface evolution, for instance, using the modified non-linear Schrödinger equation (MNLSE) (e.g. Trulsen and Stansberg, 2001). Simanesew et al. (2017) have obtained good results for unidirectional waves, although no conclusions were drawn on the practical suitability of the MNLSE to the prediction of directional wave fields. Alternatively, the high-order spectral method (HOSM) (Dommermuth and Yue, 1987; West et al., 1987) is a computationally efficient approach for modeling highly non-linear (i.e. up to any arbitrary order of non-linearity) sea states which has already been successfully employed to predict wave fields from either temporal wave probe data (Blondel et al., 2010; Qi et al., 2018a) or spatial snapshots of the surface (Klein et al., 2020; Wang et al., 2022). These prediction methods based on the HOSM have proven the importance of non-linear wave modeling on the prediction accuracy of both unidirectional and directional sea states. One crucial phenomenon, already identified in the work of Hasselmann et al. (1973) as one of the main drivers of the wave spectrum development over time, is the energy transfer resulting from non-linear wave-wave interactions (Hasselmann, 1962) appearing at the third-order of non-linear expansion. These non-linear transfers result from four-wave interaction processes, described in detail by e.g. Janssen (2004), affecting the spectral shape evolution both on short- and long-time scales for resonant and non-resonant effects, respectively. From a deterministic point of view, these four-wave interactions include the well-known modulational instability (Benjamin and Feir, 1967), participates in the creation of extreme events (Fujimoto et al., 2019) and affects significantly the dispersion relation of individual wave components. The latter effect impacts the performance of wave models in deterministic wave prediction (e.g. Meisner et al., 2023). These important contributions of third-order wave models make the third-order HOSM a good choice for wave field prediction. However, its relatively complex implementation in prediction algorithms and corresponding computational time still hinder its use in operational prediction systems for which lower-order wave models are preferred.

Since ocean waves are measured over a domain of finite size in space and time and subject to frequency dispersion, their prediction is only possible over a limited spatio-temporal region. This region is the prediction horizon and is referred here to as the predictable area. Assuming that the wave dispersion follows that of linear wave theory, Naaijen et al. (2014) and Qi et al. (2018b) have shown that the predictable area can be estimated directly from the wave spectrum of the underlying sea state. This approach relies on the assumptions that the wave spectrum is known and that wave components propagate independently, that is, without non-linear interaction. Even if weakly non-linear corrections of the wave dispersion could be taken into account, for instance by modeling third-order wave interaction effects on the group velocity (with a rather limited impact on the predictable area) (e.g., Qi et al., 2018a), all the other non-linear phenomena such as the presence of bound waves and energy transfers cannot be considered. In consequence, this approach only depicts the theoretical performance of prediction methods when linear wave assumptions are fulfilled.

In contrast, it is proposed in this paper to investigate the predictable area based on a non-linear reference wave model and to study the influence of the physical fidelity of the wave prediction modeling in different sea state configurations. In accordance with the information the analysis of marine radar measurements gives access to, it is assumed that the ocean surface dynamics is known over a limited spatial domain, and the linear wave theory and the HOSM at second, third and fourth order of non-linearity are used to propagate the surface with different levels of physical fidelity. Then, the prediction accuracy is quantified by comparing the predicted waves to a reference, i.e. a fully known wave field propagated with the HOSM at fourth order. This procedure makes it possible to track the spatiotemporal evolution of the prediction accuracy and effectively define the predictable area as the region over which the accuracy is higher than a certain threshold. This study is limited to unidirectional waves to balance the number of simulations and numerical efficiency, and the impact of the wave steepness, the water depth and wave energy spreading around the peak spectral frequency on the extent of the predictable area is investigated. At the end, the conclusions and limitations of the study are discussed.

2. Theoretical background

Under the assumptions of irrotational flow and incompressible and inviscid Newtonian fluid, the water wave problem can be described according to the potential flow theory (e.g. Mei et al., 2005). The flow velocity and pressure fields can then be derived from a scalar potential $\phi(x,z,t)$, satisfying the Laplace equation in the whole fluid domain, a non-penetration condition on the seabed (on $z=-d$) and two non-linear boundary conditions on the free surface (on $z=\zeta(x,t)$).

By applying the perturbation theory for the unknown potential ϕ and surface elevation ζ, the linear wave theory can be derived from the boundary value problem described above. The problem on the unknown surface elevation is approximated by Taylor series expansions around $z=0$. Then, under the assumption that the wave height (H) is significantly smaller than the wavelength (L), the series is truncated at the first order in wave steepness (H/L). This results in a simplified boundary value problem for which an analytical linear solution can be determined. The solution for the surface elevation of an irregular unidirectional wave field reads

$$\zeta(x,t)=\sum_n A_n\cos\left(k_n x-\omega_n t+\Theta_n\right), \tag{1}$$

where A_n represents the wave amplitude, k_n the wave number, ω_n the angular frequency and Θ_n the phase, each of the nth wave component. Linear irregular wave fields are thus described as a superposition of independent wave components that differ in amplitude, frequency and phase. Wave numbers and angular frequencies are linked via the dispersion relation

$$\omega_n=\sqrt{k_n g\tanh\left(k_n d\right)}. \tag{2}$$

enabling wave field transformations between time and space domains.

In the present work, non-linear wave field simulations are done with the HOSM, a pseudo-spectral method developed independently by West et al. (1987) and Dommermuth and Yue (1987) to solve the non-linear water wave problem. It is based on the Zakharov equation (Zakharov, 1968) and has the capability to represent many free wave components and their non-linear interactions up to any arbitrary order M in wave steepness. The formulation of the equations at the free surface using the surface velocity potential $\Psi(x,t)\equiv\phi(x,\zeta,t)$, depicts the basis for its efficiency as the fluid domain does not need to be considered. A description of the used HOSM solver is given in Lünser et al. (2022), to which the reader is referred for more numerical details. Throughout the paper, HOSM solutions are denoted HOSMX for the X^{th}-order solution.

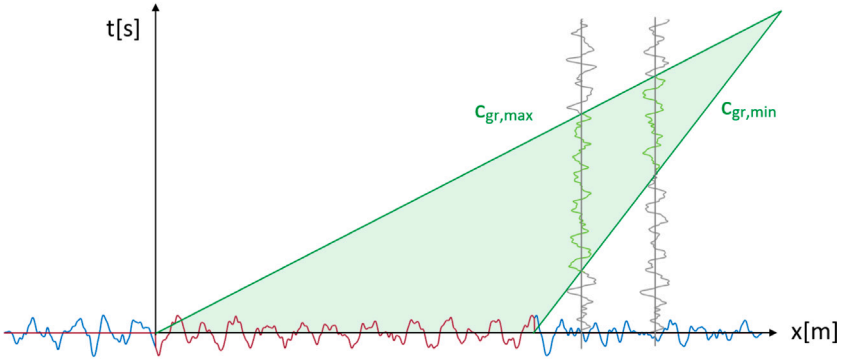

Fig. 1. Visualization of the predictable area: surface elevation in the space domain (blue curve), section of elevation as recorded by a marine radar (red curve), gauges that record the surface elevation in the time domain (gray curves), predictable area delimited by the propagation of the fastest and slowest impactful wave groups (transparent green region).

2.1. Notion of predictable area

As mentioned above, the prediction of ocean waves from a set of wave measurements is only possible over a limited spatiotemporal region referred to as predictable area. This limitation can be explained with the help of the linear wave theory for which a wave field can be viewed as a superposition of independent wave components of different frequencies and having their own amplitude and phase. To be able to predict such a wave field, the information (i.e. amplitude and phase) related to all the wave components – extracted from the measurements – have to be known at the location/time of interest. In other words, only waves whose information has been measured can be predicted. It has been shown that wave information travels at the corresponding wave group velocity c_{gr} (e.g. Naaijen et al., 2014; Qi et al., 2018b), which is different for each wave component due to frequency dispersion: long waves travel faster than short waves. In consequence, the information of the wave components disperses as the wave field propagates, leading the region over which the information of all the wave components is known to shrink and eventually disappear. By assuming that the wave spectrum is known and using an explicit expression for the dispersion relation, e.g. based on the linear wave theory or including the effects of third-order resonant interactions, it is possible to define a theoretical predictable area from the amount of known wave information in space and time (Wu, 2004).

In practice, definite borders of the theoretical predictable area are obtained by selecting two wave frequencies that correspond to the fastest and slowest wave groups whose energy is considered high enough to impact the wave field dynamics. Then, at a spatial location x, a point in time is considered to be within the predictable time range if the slowest measured wave group has arrived at x, while the fastest measured wave group has not passed x yet. Fig. 1 shows a graphical interpretation of the boundaries of the predictable area. The spatial domain is shown on the abscissa and the time domain on the ordinate. The blue curve represents the surface elevation $\zeta(x)$ and the red curve a section of it, such as recorded by a marine radar at a specific time. The gray curves represent the surface elevation in the time domain, such as recorded by two wave gauges outside the measured region and at later times. The green lines depict the propagation of the slowest and fastest wave groups (traveling along the positive x direction at $c_{gr,max}$ and $c_{gr,min}$, respectively) and delimit the predictable area (transparent green region). As can be seen, the time interval for which a prediction is possible becomes smaller with increasing distance from the measurements.

While the linear consideration of the problem is very useful to explain this phenomenon and estimate the accessible region for prediction, it does not take into account the potential error of the wave modeling with respect to the non-linear physics of the underlying wave field. In real world applications, the predictable area will depend strongly on the validity of the applied modeling as inaccurate models will increase the prediction error in space and time. Using a selection of wave models, this paper aims to quantify the impact of this modeling error on the prediction accuracy and define a predictable area that better represents the expected performance of different prediction methods.

3. Setup of numerical experiment

The focus of the numerical experiments was on investigating the impact of three physical effects on the predictable area: first, the influence of increasing wave steepness and thus wave field non-linearities; second, the shape of the spectrum in terms of spectral bandwidth; and third, the influence of decreasing water depth on wave propagation. For this purpose, three different water depths, four different wave steepness values and two different spectral bandwidths based on the enhancement factor of the JONSWAP spectrum were investigated resulting in 24 different sea state combinations (taking the different water depths into account). In addition, 100 random realizations were initialized for each combination to obtain an averaged estimation. Simulations of each sea state combination were carried out with linear wave theory and HOSM4 for the full snapshot (i.e. reference) as well as with linear wave theory, HOSM2, HOSM3 and HOSM4 for the radar-equivalent cutout wave field (i.e. prediction) to obtain time series of surface elevation at five different positions in the direction of wave propagation ($\Delta x = \{1, 2.5, 5, 7.5, 10\} \cdot L_p$ with L_p the peak wavelength of the sea state spectrum). The results obtained are evaluated by comparing the predictions with the reference HOSM4 (and linear wave theory) solution.

3.1. Wave field definition

The initial unidirectional irregular sea states were calculated based on the JONSWAP TMA spectrum (Hasselmann et al., 1973; Bouws et al., 1985) and reads

$$S_\zeta(\omega) = f_k(\omega) \cdot \frac{\alpha g^2}{\omega^5} \cdot \exp\left[-\frac{5}{4} \cdot \left(\frac{\omega_p}{\omega}\right)^4\right] \cdot \gamma^{\exp\left[-\frac{(\omega-\omega_p)^2}{2b^2\omega_p^2}\right]}, \tag{3}$$

where S_ζ is the spectral energy density, α is the Phillips coefficient which depends on the characteristic wave steepness, ω_p is the peak angular frequency (i.e. of maximum energy), γ is the spectral peak enhancement factor and $b = 0.07$ for $\omega < \omega_p$ or 0.09 otherwise. $f_k(\omega)$ represents the finite-depth correction,

$$f_k(\omega) = \frac{\tanh^2(kd)}{1 + {}^{2kd}/_{\sinh(2kd)}}, \tag{4}$$

with the angular frequency ω and wave number k being linked via the linear dispersion relation (cf. Eq. (2)). Four predefined values of wave steepness $\epsilon = k_p H_s/2$ were investigated, with k_p the peak wave number (linked to ω_p via linear dispersion relation) and H_s the significant wave height. The smallest investigated wave steepness is $\epsilon = 0.0125$ and the

Table 1
Overview of evaluated sea states.

Sea state	T_p	ϵ	γ
1	8 s	0.0125	1
2			6
3		0.025	1
4			6
5		0.05	1
6			6
7		0.1	1
8			6

highest $\epsilon = 0.1$, representing small to steep waves. The width of the spectra was limited to $k_{max} = 6 \cdot k_p$ to avoid numerical instabilities of the HOS method for the highest wave steepness, i.e. to suppress high-frequency contamination that can occur for the highest waves. In addition, two peak enhancement factors, $\gamma = 1$ and $\gamma = 6$, were used to represent different spectral bandwidths. Last but not least, three different water depths were selected for each sea state parameter combination: $d = 5000\,\text{m}$ ($k_p d = 314.4$), $d = 40\,\text{m}$ ($k_p d = 2.55$) and $d = 30\,\text{m}$ ($k_p d = 1.96$). The different water depths, particularly the two intermediate water depths, were chosen in order to model the water depth conditions in the North Sea. For every evaluated sea state per water depth, summarized in Table 1, the peak period $T_p = 8\,\text{s}$ was kept constant.

3.2. Wave field simulation

Fig. 2 shows the numerical setup for an exemplary initial sea state. The total simulation area had a length of 5000 m. The periodic domain was discretized by $N = 2^{11}$ grid points for all simulations, resulting in a spatial resolution of 2.44 m. The simulation time was set to 600 s with a temporal resolution of 0.05 s. For each sea state combination from Table 1 and the three different water depths, simulations were performed as followed:

- Based on the respective sea state parameters and water depth, the corresponding JONSWAP TMA spectrum was determined. Hereby, Rayleigh distributed random amplitudes based on the respective JONSWAP TMA spectrum solution following DNV-RP-C205 (2023) were applied to take the randomness of natural seaway spectra into account. In order to ensure that the area under the Rayleigh distributed amplitudes represent the targeted significant wave height, 1000 random realizations of the amplitude spectrum were calculated and the one closest to the targeted significant wave height were used in the following ($H_s - 4 \cdot \sqrt{m_0} \leq 10^{-5}$). Afterwards, the JONSWAP TMA spectrum was transformed into space domain applying random phases between $-\pi \leq 0 \leq \pi$.
- Based on the space domain realization of the JONSWAP TMA spectrum, the initial spatial snapshot that extends over the entire domain (blue curve in Fig. 2) were generated using linearly initialized HOSM4 simulations in which non-linearities were progressively turned on, following the procedure explained by Dommermuth (2000). This so-called relaxation procedure avoids the creation of numerical artifacts during the wave field evolution, and ensures the generation of a physically consistent non-linear HOSM solution, i.e., the initial wave field for the following investigations represents a non-linear (4th-order) fully evolved initial wave field.
- The non-linear fully evolved initial spatial snapshot was afterwards used to simulate the reference solutions (HOSM4 and linear wave theory) in time at the five different wave gauge positions. For the HOSM4 simulation, the resulting non-linear wave elevation and corresponding 4th-order non-linear potential was used as starting point whereas the non-linear surface elevation was exclusively used for the linear wave simulation.
- As a next step, only a section of the initial snapshot, ranging from $x = 1000\,\text{m}$ to 3500 m with zero-valued quantities elsewhere (red curve in Fig. 2) as well as the same section extended with the NewWave solution (green curve in Fig. 2), was selected as a basis for wave field predictions with the linear wave theory, HOSM2, HOSM3 and HOSM4. For the propagation of the sections with HOSM, the initial non-linear surface elevation was extracted from the initial non-linear HOSM4 snapshot, whereas the surface velocity potential was approximated from the non-linear elevation using the linear wave theory. This is an appropriate approach for an application-oriented prediction scenario, as numerical efficiency is an essential aspect of the predictable area. The dimension of the selected surface section reflects the measurement range of marine radars.

3.3. Smoothing using the NewWave group

Hlophe et al. (2021) have found that "introducing a smooth transition of the record down to zero at both ends by adding half of a NewWave-type wave group improves the prediction at the point of interest dramatically compared to just using the raw record". The NewWave has been developed by Tromans et al. (1991) "as a representation of the most probable extreme wave" to determine "the surface elevation and water particle velocities and accelerations induced by extreme ocean waves". The idea of Hlophe et al. (2021) is to extend each end of the selected section of the surface using a wave group that smoothly goes to zero according to the following NewWave solution

$$\zeta_{NW}(x,t) = \frac{a}{m_0} \sum_n S_\zeta(\omega_n)\, \Delta\omega_n \cos\left(k_n x - \omega_n t\right), \tag{5}$$

where a is the amplitude at the section end and m_0 is the zeroth-order moment of the spectrum. They have studied "single, fixed-probe measurements for predicting unidirectional wave fields" with linear and weakly non-linear simulations. Here, to investigate whether their findings apply to input spatial snapshots instead of probe measurements, simulations were carried out in which the initial solution was extended with one half of the NewWave at both ends (green curve in Fig. 2).

3.4. Error analysis

In this study, the Surface Similarity Parameter (SSP) (Perlin and Bustamante, 2016) was used as an error indicator. From two input signals ζ_1 and ζ_2, the SSP always ranges between 0 (perfect agreement) and 1 (perfect disagreement) and is calculated as

$$\text{SSP} = \frac{\left(\int |F_1(\omega) - F_2(\omega)|^2 \mathrm{d}\omega\right)^{\frac{1}{2}}}{\left(\int |F_1(\omega)|^2 \mathrm{d}\omega\right)^{\frac{1}{2}} + \left(\int |F_2(\omega)|^2 \mathrm{d}\omega\right)^{\frac{1}{2}}}, \tag{6}$$

where $F_{1,2}(\omega)$ are the temporal Fourier transforms of the signals $\zeta_{1,2}$. For this study, the accuracy was assumed to be acceptable as long as SSP≤ 0.1, which defines the threshold accuracy of the predictable area. As an example, the bottom diagram in Fig. 3 presents a comparison of two signals for which SSP = 0.1. Note that not only the extent of the predictable area (defined by the threshold) but also the curves of the SSP variations are given in the results section in order to depict the full picture of the prediction accuracy. By doing so, the extent of the predictable area for other threshold values can be visually inferred.

For all initial conditions described, the surface elevation $\zeta(t)$ was determined at five gauge positions, located at distances from the closer edge of the radar snapshot $\Delta x = \{1, 2.5, 5, 7.5, 10\} \cdot L_p$ (with L_p the peak wavelength of the sea state spectrum; see the vertical lines in Fig. 2) over the simulation time of 600 s. Note that the absolute distance of the wave gauges differ slightly for the different water depths as the peak wavelength is affected by the water depth (cf. Eq. (2)) and the gauge positions in Fig. 2 are shown for the deep water case for illustrative

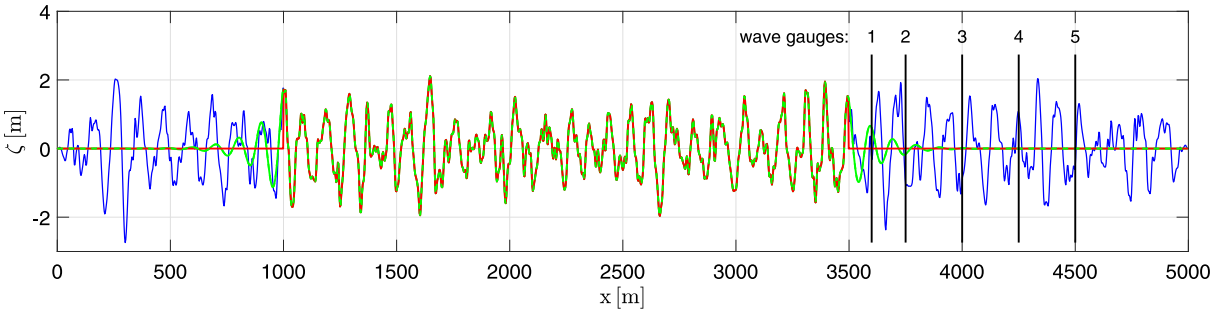

Fig. 2. Numerical setup for an exemplary sea state, with the surface elevation (blue curve), the selected section (red curve) and the section extended with the NewWave solution (green curve). The wave gauges for the prediction accuracy analysis (vertical lines) are located downstream, outside the selected section.

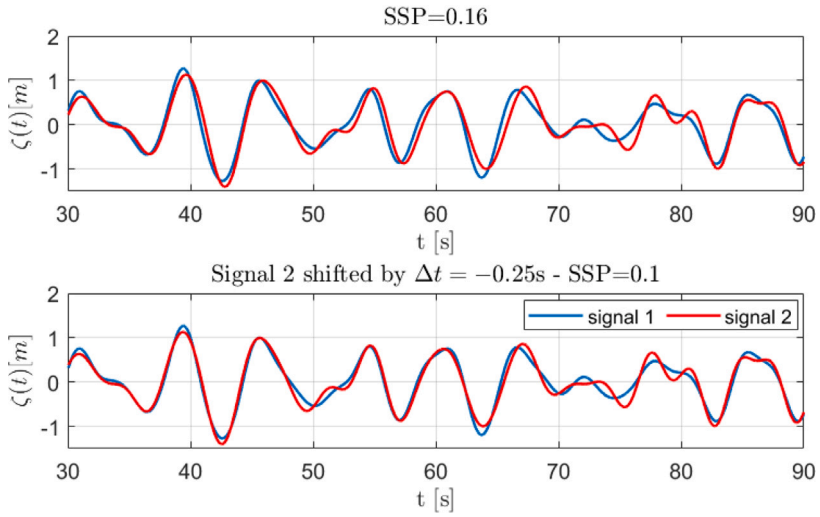

Fig. 3. Exemplary comparison of two signals to get an impression of an agreement of SSP = 0.1 and the effect of the signal shift on the SSP.

purposes. These time series, corresponding to the reference surface and to (non-linear) predictions, were then compared to calculate the SSP. To quantify the SSP as a function of time at the wave gauge locations and identify the start and end of the predictable area, the signals compared in Eq. (6) were taken according to a sliding time window approach. Considering that prediction methods from radar data should be able to perform at least one-minute long predictions, the size of the sliding window was set to 60 s and the shifting step along the time series to 1 s.

To ensure that a certain proportion of the calculated error between the two signals of 60 s is not only due to a pure phase shift, as expected for the wave models with less complexity (e.g. linear wave theory and HOSM2) and increasing wave steepness, the smallest SSP between the two signals was determined by shifting one time series relative to the other by $-3\,\mathrm{s} \leq \Delta t \leq 3\,\mathrm{s}$ with a resolution of 0.05 s. Fig. 3 illustrates the approach exemplarily. The top diagram presents the comparison between two signals without a time shift resulting in SSP = 0.16. The bottom diagram shows the same signals where signal 2 has been shifted by $\Delta t = -0.25\,\mathrm{s}$ resulting in SSP = 0.1. With this approach, the discrepancy between two signals due to different modeling complexity of the underlying wave dispersion can be compensated at least on an average level. From an application-orientated point of view, this is acceptable for most case as the identification of critical wave heights/groups for a certain duration is required. For applications that require wave predictions as basis for active control algorithm, the situation may be different. The impact of wave steepness on the magnitude of the time/phase shift of the different wave models is discussed in detail in Section 4.

For each one of the 8 sea state combinations given in Table 1 and the three different water depths, 100 simulations with random initializations were performed before calculating the mean value of the error indicator. This procedure allowed statements to be made independently of particularities of each wave field realization, for instance a surface truncation being made at a deflection of zero.

4. Results and discussions

4.1. Interpretation of the results

Using a sliding window for the calculation of the SSP requires to interpret the results as follows — in the following figures, the SSP value is plotted in the middle of each 60 s sliding window. This denotes that, for example, the value of the 60 s to 120 s section is plotted at 90 s. Therefore, this value does not apply from 90 s onwards, as might be assumed at a first glance, but from 60 s to 120 s. Fig. 4a shows an exemplary course of the SSP (red curve) and additionally for each data point the size of the sliding window (black lines), which mark the time range for which the SSP in the middle applies. In the depicted case, the SSP is below the defined threshold of SSP = 0.1 (see Section 3.4) between 75 s and 270 s, thus the predictable area in this example starts at 75 − 30 = 45 s and ends at 270 + 30 = 300 s. In addition, in order to improve the readability of the results, the areas that fall below the defined threshold of SSP = 0.1 are displayed as a block (see Fig. 4b). In this representation, the time can be read exactly as shown, since the 30 s are added at both ends.

The results are referenced according to the two methods used to generate the predicted and reference surfaces. The model of the predicted surface is mentioned first, then that of the reference surfaces. The abbreviation “NW” means that the surface smoothing using the NewWave group was applied (see Section 3.3). For example, the label

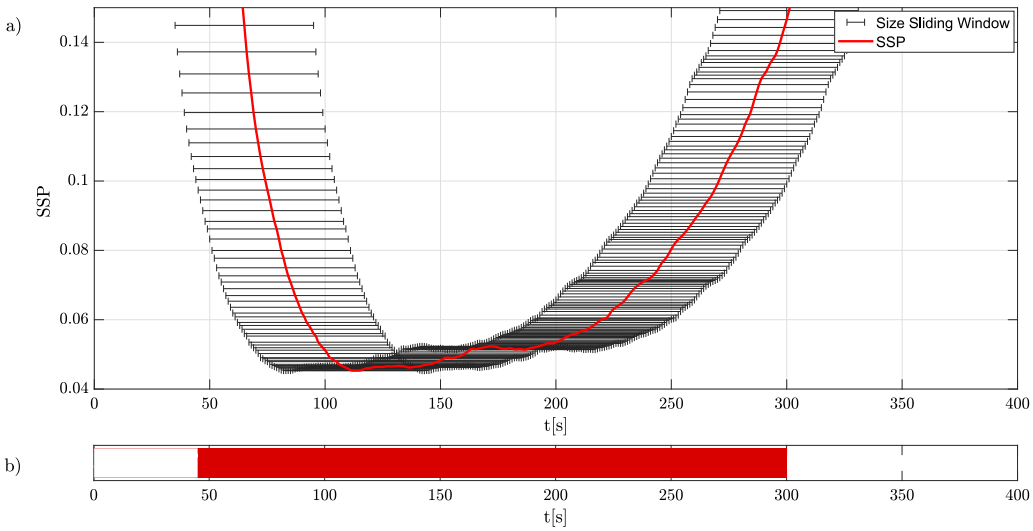

Fig. 4. (a) Exemplary SSP (red curve) and corresponding size of the sliding window (black lines). (b) The same data, but in a more readable representation: only the section below the threshold of 0.1 is shown as a block.

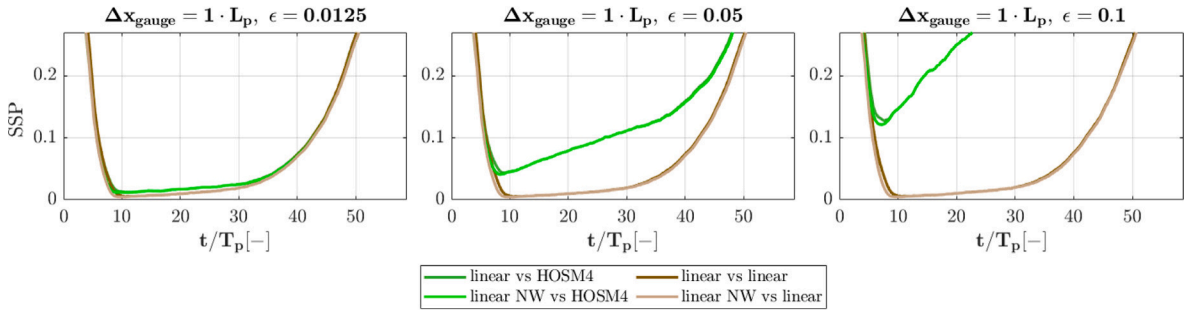

Fig. 5. SSP obtained for linear predictions in deep water compared to both linear (brown curves) and non-linear (green curves) reference surfaces. Results obtained with (light curves) and without (dark curves) the NewWave smoothing are presented.

"linear NW vs HOSM4" means that the prediction was performed with linear wave theory including the NewWave smoothing, while the reference surface was simulated with HOSM4.

4.2. Influence of non-linear reference solution

Following, the influence of the non-linear nature of the reference solution on the predictable area is investigated. Fig. 5 compares the prediction accuracy at one specific location $\Delta x = 1 \cdot L_p$ in deep water conditions for different wave steepness values. The wave steepness increases from left to right and the spectral peak enhancement factor was set to $\gamma = 1$.

For linear predictions with a linear reference solution (linear (NW) vs linear — brown curves), the wave steepness has no effect on the results since linear wave theory does not represent non-linear effects. Linear predictions with a non-linear reference solution (linear (NW) vs HOSM4 — green curves) reveal that the accuracy of the linear modeling is suitable for the smallest investigated steepness, but decreases significantly with increasing steepness in terms of overall accuracy as well as predictable area. This highlights the motivation of the present study and already indicates that the determination of the predictable area based on linear reference solution may lead to strong misinterpretation for practical applications in sea states with moderate and steep waves.

Results from the NewWave group smoothing are shown in Fig. 5 to evaluate the benefit of this approach in the presented configuration. As stated in Hlophe et al. (2021), Fig. 5 indicates that the surface smoothing with the NewWave group has a positive impact on the linear predictions (dark curves compared to light curves), although it is not significant here. Generally, a similar impact of the NewWave group smoothing was also observed for the predictions based on the HOSM simulations (but not shown to keep Fig. 5 simple) as well as all sea state realizations, water depths and wave gauge locations. The main reason for marginal impact compared to the overall predictable area lies in the fact that the HOS method was implemented with a low-pass filter to avoid Fourier space aliasing and to ensure numerical stability for the steepest sea states (West et al., 1987). As such a filter results in a smoothing effect at the sudden cuts, it already had a positive influence similar to the NewWave group smoothing approach. This filter was also applied to the linear approach to obtain a consistent basis for comparison, hence, the surface smoothing had only a limited impact on the linear predictions as well. However, without the filter, the NewWave smoothing had a more pronounced effect being consistent with the findings of Hlophe et al. (2021). Since the generation of the NewWave required an extra computational effort for a small benefit for the presented investigations, it is not further discussed in the following.

4.3. Influence of the wave steepness and prediction distance

Fig. 6 presents the prediction accuracy of linear vs HOSM4 (green), HOSM2 vs HOSM4 (black) and HOSM3 vs HOSM4 (red) predictions for all sea states and gauge positions ($\gamma = 1$; Fig. 12 for $\gamma = 6$). The solid curves represent deep water conditions, the dashed curves $d = 40\,\mathrm{m}$ and the dotted curves $d = 30\,\mathrm{m}$. The wave steepness is kept constant vertically, increasing from left to right, and the distance is kept constant horizontally, increasing from top to bottom. The position of the wave

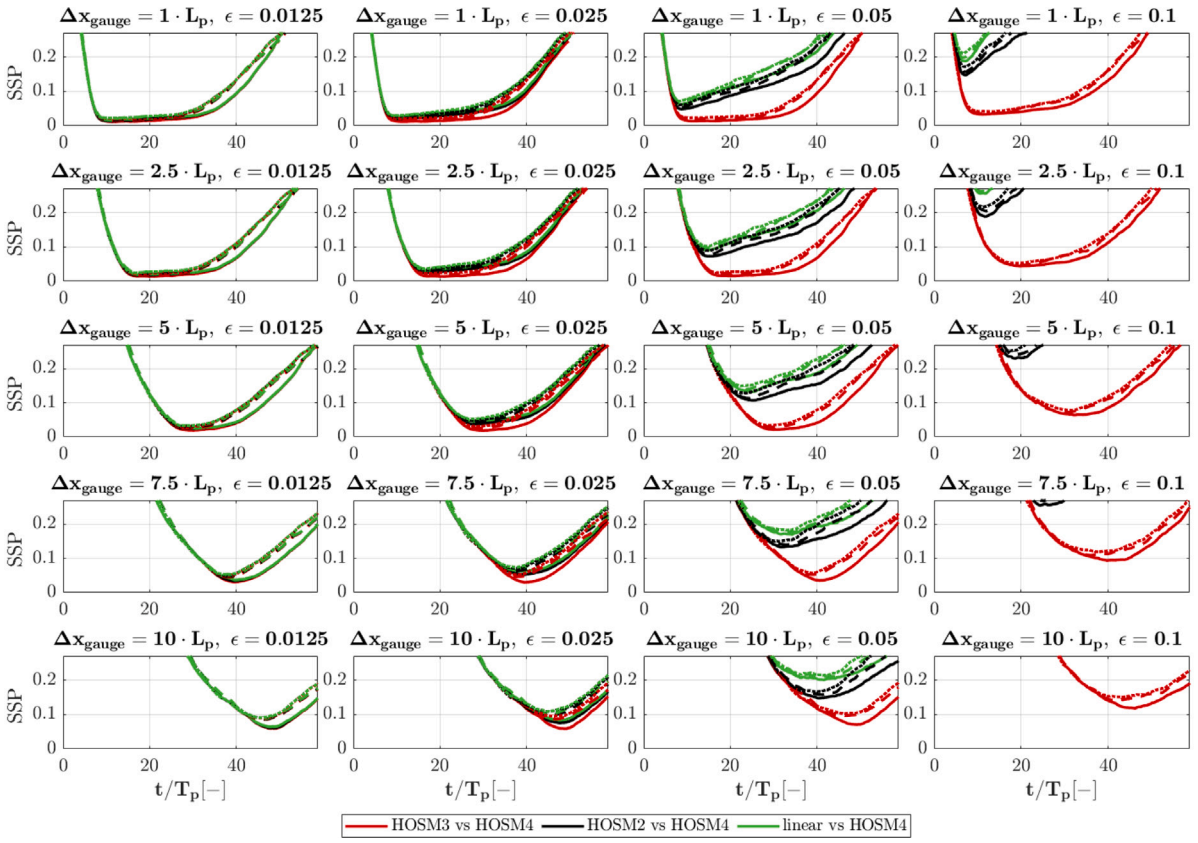

Fig. 6. SSP for all evaluated sea states (Table 1) for $\gamma = 1$. The wave steepness is kept constant vertically and increases from left to right. Horizontally, the prediction distance (see the gauge locations in Fig. 2) is kept constant and increases from top to bottom.

gauges (expressed in terms of number of peak wave wavelengths of the sea state) and the respective wave steepness are shown in the title of each sub-figure. The abscissa presents the SSP and the ordinate the time normalized with the peak wave period. These results show that the prediction accuracy decreases with increases distance and wave steepness for all methods, which is significantly more pronounced for the linear approach and HOSM2. The linear approach results in a similar accuracy to that of the non-linear approaches for the smallest steepness ($\epsilon = 0.0125$) over all distances. Even for the second smallest steepness ($\epsilon = 0.025$), the linear approach provides sufficient model accuracy compared to the non-linear approaches. With increasing steepness, the linear approach starts to differ significantly. However, this shows the operational capability of the linear approach for deterministic wave prediction being sufficient for certain application ranges. HOSM2 results perform slightly better for the second smallest steepness compared to the linear approach but also show a decreased accuracy for the two highest wave steepness. As expected from the modeling of four-wave interactions, which include the most impactful phenomena in non-linear wave propagation (e.g. Hasselmann, 1962; Janssen, 2004), HOSM3 provides the best prediction accuracy over a wide range of steepness values and distances. Fig. 6 already highlights the importance of the order of the considered wave model in terms of accuracy and predictable area.

Analyzing the impact of the water depth on the prediction accuracy and horizon reveals that the course of the SSP at the beginning is similar to the deep-water case but does not fully reach the same accuracy. Furthermore, the accuracy decreases faster compared to the deep-water case resulting in a shorter predictable area. This behavior becomes more pronounced for larger prediction distances, larger wave steepness and decreasing water depth. The shorter predictable area can be explained by the water depth influence on the group velocity. For wavelength in the intermediate water depth regime, the group velocity increases with decreasing water depth. In terms of predictable area, this denotes that the beginning of the predictable area is unaffected (in this study) as this is related to the slowest/shortest wave group (still in deep water condition) reaching the prediction location, but the end of the predictable area, which is related to the fastest/longest wave group, is significantly affected (cf. Fig. 1 and Section 4.5). The fact that the overall prediction accuracy in intermediate water decreases with decreasing water depth can also be explained by the impact of the water depth on the group velocity as the fastest/longest wave groups inside the wave sequence travel faster outside the wave sequence as well as the fastest/longest wave groups outside the wave sequence are traveling faster inside the wave sequence and predictable area. In addition, the analysis showed that decreasing the water depth also had an influence on the numerical simulation of the wave sequence sections. By decreasing the water depth as well as increasing the steepness and prediction distance, numerical artifacts in the area of the first harmonics in frequency domain, i.e. extremely long wave contributions, were observed with a clear impact on the overall simulation accuracy. This is discussed in more detail in Section 4.6.

Based on Figs. 6, 7 shows the corresponding predictable areas ($\gamma = 1$; Fig. 13 for $\gamma = 6$), determined as explained in Section 3.4. Besides the three cases presented in Fig. 6, results pertaining to the linear vs linear and HOSM4 vs HOSM4 predictions are given to obtain a more complete overview. Fig. 7 displays the same trend as shown in Fig. 6 with a focus on the predictable area for a defined minimum prediction accuracy (SSP ≤ 0.1), i.e. the predicable area decreases with increasing wave steepness. However, the range of application of the different models can be assessed more clearly due to the defined minimum prediction accuracy that gives new insights. First, Fig. 7 confirms that all the models shown are applicable for the two smallest wave steepness values investigated over almost all distances. However, the furthest distance $\Delta x = 10 \cdot L_p$ for $\epsilon = 0.025$ already indicates that the low-order models

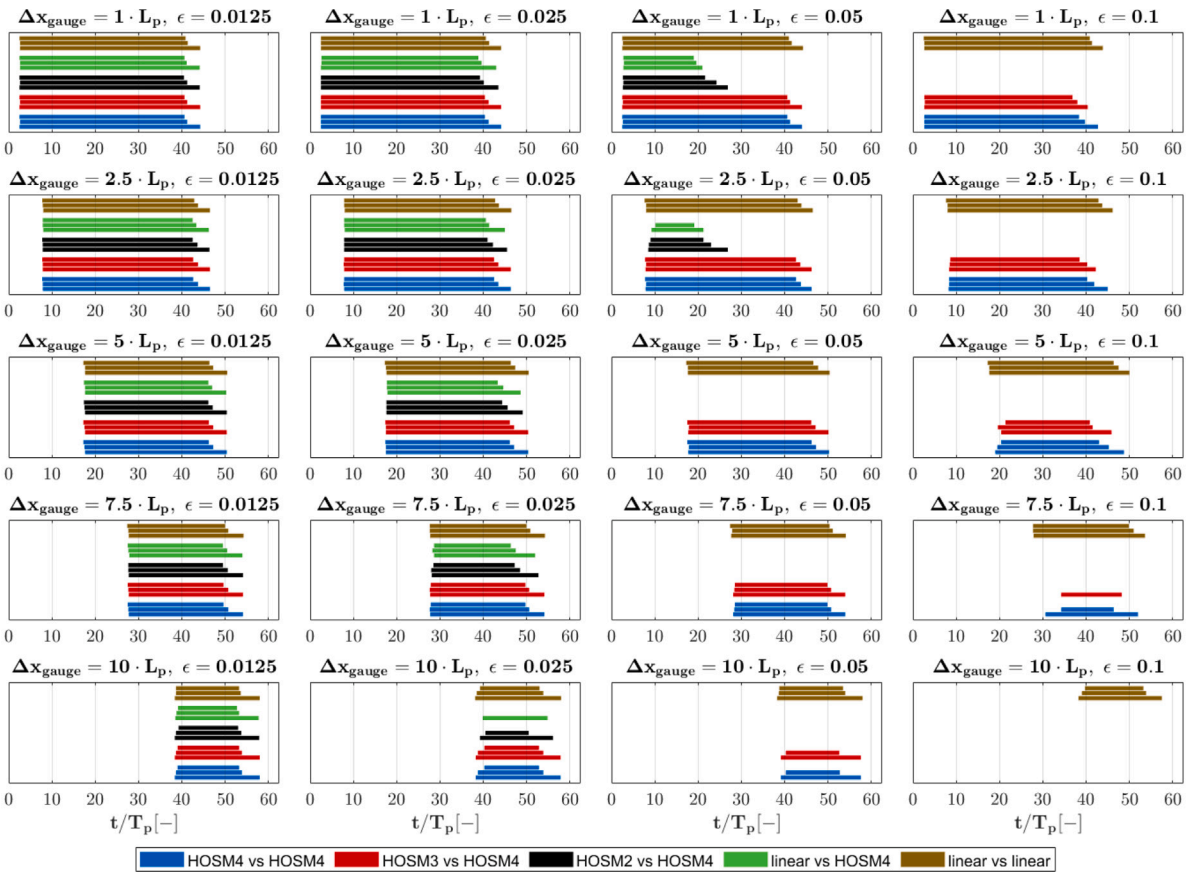

Fig. 7. Predictable area for all investigated sea states for $\gamma = 1$. The wave steepness is kept constant vertically and increases from left to right. Horizontally, the prediction distance (see the gauge locations in Fig. 2) is kept constant and increases from top to bottom.

are reaching their limits — the predictable area of linear vs HOSM4 and HOSM2 vs HOSM4 are starting later and ending earlier. For the two intermediate water depth cases, the prediction accuracy is already above the defined minimum prediction accuracy (SSP ≤ 0.1). For steepness $\epsilon = 0.05$, the results of the linear approach and HOSM2 differ strongly from those of HOSM4, yielding a predictable area below the threshold only for the two shortest distances and significantly shorter compared to HOSM3. This highlights the importance of modeling third-order effects, which significantly influence the wave dynamics. The accuracy of HOSM3 is similar to that of HOSM4 in a wide range of investigated configurations, differing only for the highest wave steepness and two farthest distances, which is consistent with earlier findings in Lünser et al. (2022). In addition, all models are not able to make predictions for the highest wave steepness and prediction distance — it should be noted that this result is specifically valid for $\gamma = 1$ (see Section 4.4 and Appendix).

The discussed effect of the intermediate water depth on the predictable area can be clearly seen in Fig. 7. The beginning of the predictable area is, as already discussed, more or less identical for all water depths, particularly for the shorter prediction distances; small deviations are recognizable, which can be explained by the temporal resolution of the sliding window. For steeper wave sequences and farther distances, respectively, the predictable area tends to start later. For the end of the predictable area, the impact of the intermediate water depth on the group velocity results in a shorter predictable area with decreasing water depth. Again, this observation also seems to increase with increasing steepness and distance. Both can be explained with the observed discrepancy in the accuracy reached for the different water depths: for the steepest cases and farthest prediction distances, the course of the accuracy curves (cf. Fig. 6) is further flattened, which is why the threshold is reached later or exceeded again earlier. For some case, the accuracy threshold is not even reached for specific water depths, whereas the deep water case still reaches the threshold. In this context, the steepest case with the two farthest prediction distances is also very challenging for HOSM3, and even the HOSM4 predictions, which has the same model order as the reference sea state, are outside the accuracy threshold for the steepest and farthest prediction distances case. Particularly noteworthy is that the predictable area of HOSM3/HOSM4 vs HOSM4 is very similar to that of the linear vs linear case for a wide range of investigated steepness values and prediction distances, even if this may be related to the selected minimum prediction accuracy.

4.4. Influence of the peak enhancement factor

In this section, the influence of the peak enhancement factor on the predictable area is discussed. Fig. 8 presents the prediction accuracy of linear vs HOSM4, HOSM2 vs HOSM4 and HOSM3 vs HOSM4 for two peak enhancement factors, two different steepness values and two prediction distances — the distance increases from top to bottom and the wave steepness from left to right. Solid lines present the results for $\gamma = 1$ and dotted lines for $\gamma = 6$, in each case for linear vs HOSM4 (green), HOSM2 vs HOSM4 (black) and HOSM3 vs HOSM4 (red). It can be seen that with increasing peak enhancement factor the accuracy increases as well. Moreover, at a large prediction distance (bottom plots), the minimum of the SSP curves is obtained less abruptly for $\gamma = 6$, which also tends to make the predictable area start earlier. Because the predictable area is directly related to the difference of propagation speed between the fastest and slowest wave groups influencing the wave dynamics, both observations can be explained by the fact that energy dispersion is less significant for narrower spectra, as it is concentrated within a narrower frequency band. The limiting case being regular waves, which

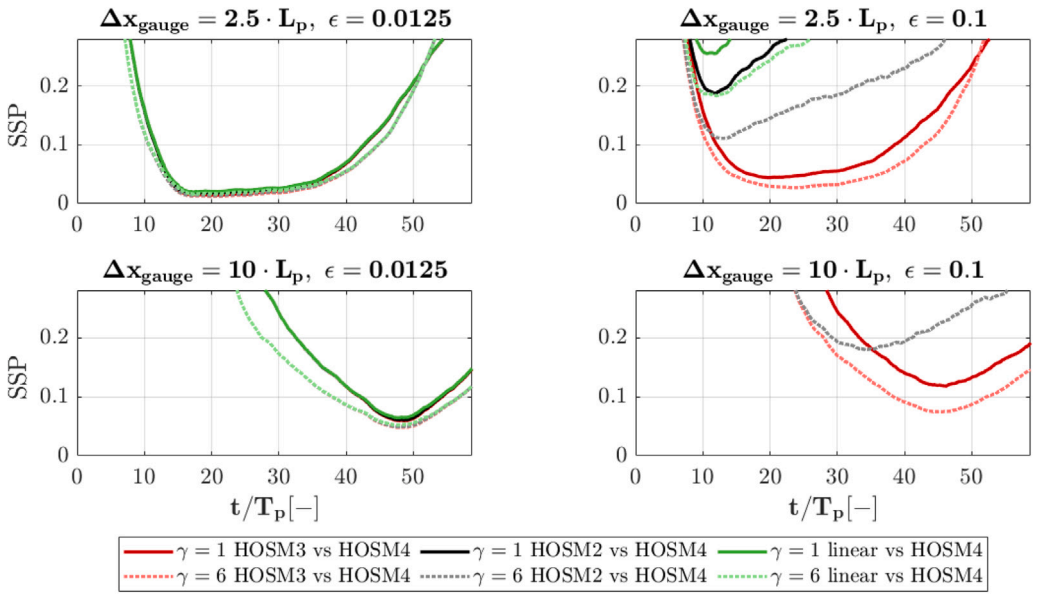

Fig. 8. Influence of the peak enhancement factor γ on the SSP for $\gamma = 1$ (solid curves) and for $\gamma = 6$ (dotted curves).

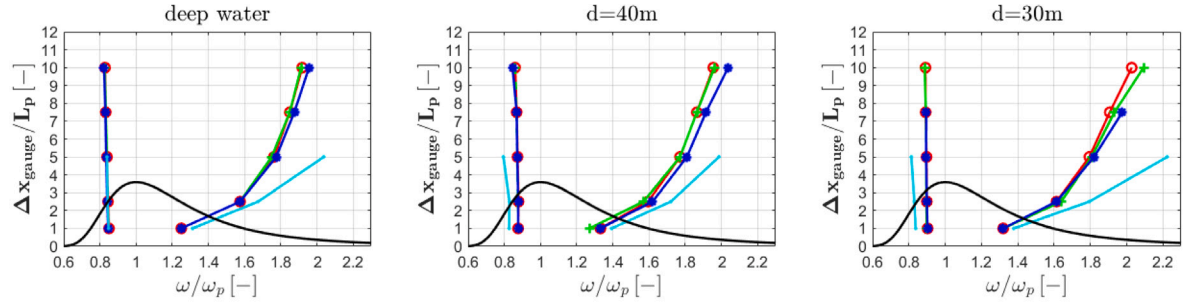

(a) Results for enhancement factor $\gamma = 1$.

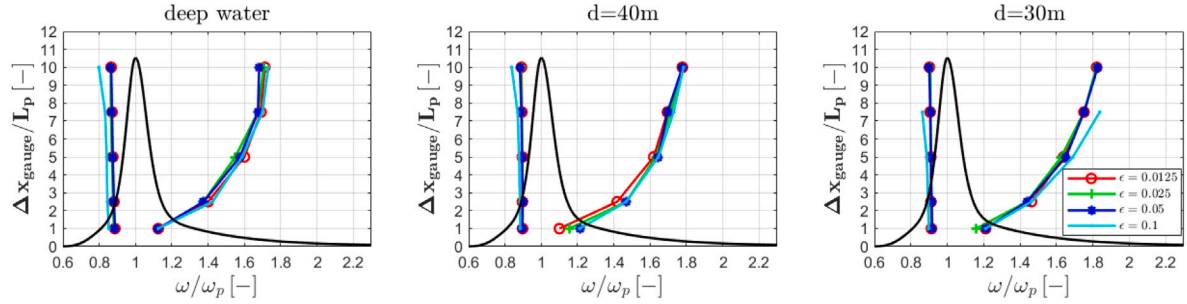

(b) Results for enhancement factor $\gamma = 6$.

Fig. 9. Limiting angular frequencies for all investigated parameters of wave steepness and prediction distance for HOSM3 vs HOSM4. The left diagram presents the results for deep water, the center diagram for $d = 40\,\mathrm{m}$ and the right diagram for $d = 30\,\mathrm{m}$ The abscissa of each diagram presents the angular frequency normalized with the peak angular frequency and the ordinate the distance to the different gauge positions normalized with the peak wavelength. In all diagrams, a normalized JONSWAP spectrum with the respective enhancement factor is shown exclusively for illustrative purpose.

can be predicted over an infinitely large predictable area (assuming that the wave dynamics is correctly modeled) due to the absence of energy dispersion, i.e. all waves propagate at the same speed.

The fact that, using HOSM3, the highest investigated wave steepness with the largest prediction distance still leads to SSP ≤ 0.1 for $\gamma = 6$ denotes that the application range of deterministic wave prediction is increased significantly for narrower spectra. The results for all sea states and water depths with $\gamma = 6$ are presented in Appendix, i.e. all figures specifically shown for $\gamma = 1$ in the paper are also plotted for $\gamma = 6$ in Appendix (Fig. 12 — Fig. 15).

4.5. Estimation of limiting wave groups

Following, the presented results are used for an application-oriented identification of the limiting wave groups defining the predictable area for varying wave steepness values, water depths and prediction distances. Predictable area refers to a certain prediction accuracy within a wave prediction time series (see Section 2.1). The identification of the area of certain prediction accuracy is essential from an application point of view, ensuring that decisions are based on reliable data. Results from Figs. 7 and 13 are the basis of the following investigation and the objective is to identify a relation between the peak frequency of the

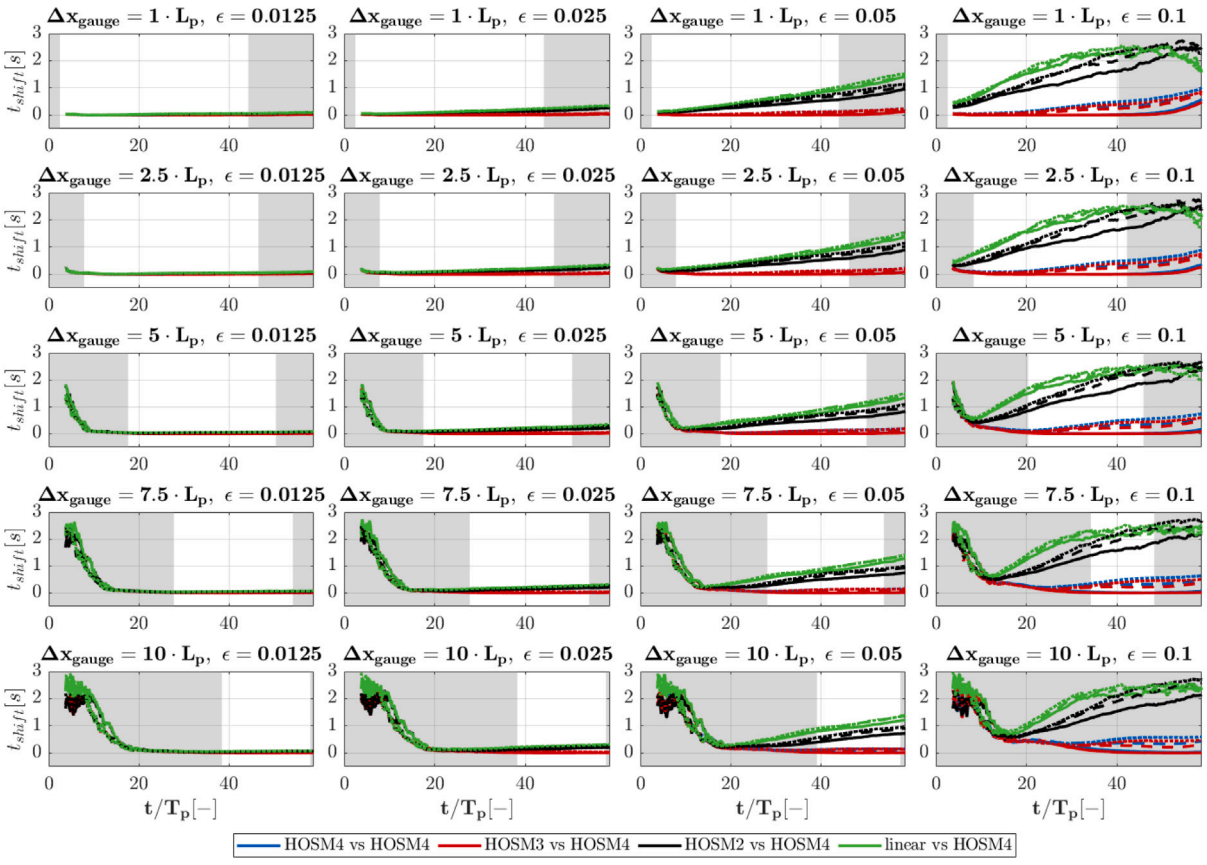

Fig. 10. Optimal time shift for all evaluated sea states (Table 1) and water depths for $\gamma = 1$. The wave steepness is kept constant vertically and increases from left to right. Horizontally, the prediction distance (see the gauge locations in Fig. 2) is kept constant and increases from top to bottom.

surrounding sea state and the wave angular frequencies of the fastest and slowest wave groups to be considered for the determination of the boundaries of the predictable area. Knowing how these limiting frequencies evolve with the prediction distance and wave steepness, it becomes possible to infer the extent of the accessible predictable area from sea state and measurement characteristics without running numerical simulations.

The slowest wave group is defined as the first waves of the initial snapshot that reach the prediction location, and is thus associated with the time t_{min} corresponding to the beginning of the bars in Figs. 7 and 13. The fastest wave group is defined as the last waves of the initial snapshot that leave the prediction location, and is thus associated with the time t_{max} corresponding to the end of the bars in Figs. 7 and 13.

Using the distances traveled by the slowest and fastest wave groups, i.e. $x_{min} = \Delta x_{gauge}$ and $x_{max} = \Delta x_{gauge} + l_{section}$, respectively, the corresponding limiting velocities $c_{gr,min}$ and $c_{gr,max}$ (see Section 2.1) can be calculated. In arbitrary water depth, the limiting group velocities can be associated with certain angular frequencies according to Eq. (2),

$$c_{gr} = \frac{c}{2}\left[1 + \frac{2kd}{\sinh(2kd)}\right], \tag{7}$$

and

$$c = \sqrt{\frac{g}{k}\tanh(kd)}. \tag{8}$$

Fig. 9 presents the limiting angular frequencies for all investigated values of wave steepness, water depths, and prediction distance for HOSM3 vs HOSM4. The top diagrams present the results for a spectral enhancement factor $\gamma = 1$ and the bottom diagrams for $\gamma = 6$. The left diagrams show the deep water results, the center diagram the $d = 40\,\mathrm{m}$ water depth case and the right diagrams the $d = 30\,\mathrm{m}$ water depth case. The abscissa presents the angular frequency normalized with the peak angular frequency and the ordinate the distance to the different gauge positions normalized with the peak wavelength. In all diagrams, a normalized JONSWAP spectrum with the respective enhancement factor is shown exclusively for illustrative purposes. Note that the slowest wave group velocity ($c_{gr,min}$) corresponds to a maximum angular frequency (ω_{max}) and the fastest wave group velocity ($c_{gr,max}$) corresponds to a minimum angular frequency (ω_{min}). In addition, the maximum possible predictable area is reached when the minimum and maximum limiting frequencies are equal to the peak frequency, i.e. the predicable area decreases with increasing distance to the peak frequency.

Analyzing Fig. 9 reveals that the ω_{min} is significantly less affected by increasing prediction distance compared to ω_{max}, for which the predictable area decreases significantly with increasing distance. The effect of the wave steepness on the predictable area is limited for moderate sea state ($\epsilon \leq 0.05$), but the general trend, that the predicable area decreases with increasing steepness, is particularly visible for $\gamma = 1$ and maximum angular frequency. For the largest investigated wave steepness, the predictable area decreases significantly. As discussed above, this effect is particular significant for $\gamma = 1$, as no accurate predictions were possible for the steepest waves and largest distances. This is less pronounced for $\gamma = 6$, but the same trend is visible.

These results imply that the traditional method for the determination of the accessible prediction zone based on a fixed amount of truncated energy is not optimal and, as already noted in previous studies, conservative and leading to underestimate the predictable area (e.g. Huchet et al., 2023; Desmars et al., 2023).

4.6. Discussion on the identified time shift

As discussed in Section 3.4, the smallest SSP between the reference solution and the prediction (consecutive time windows of 60 s) was

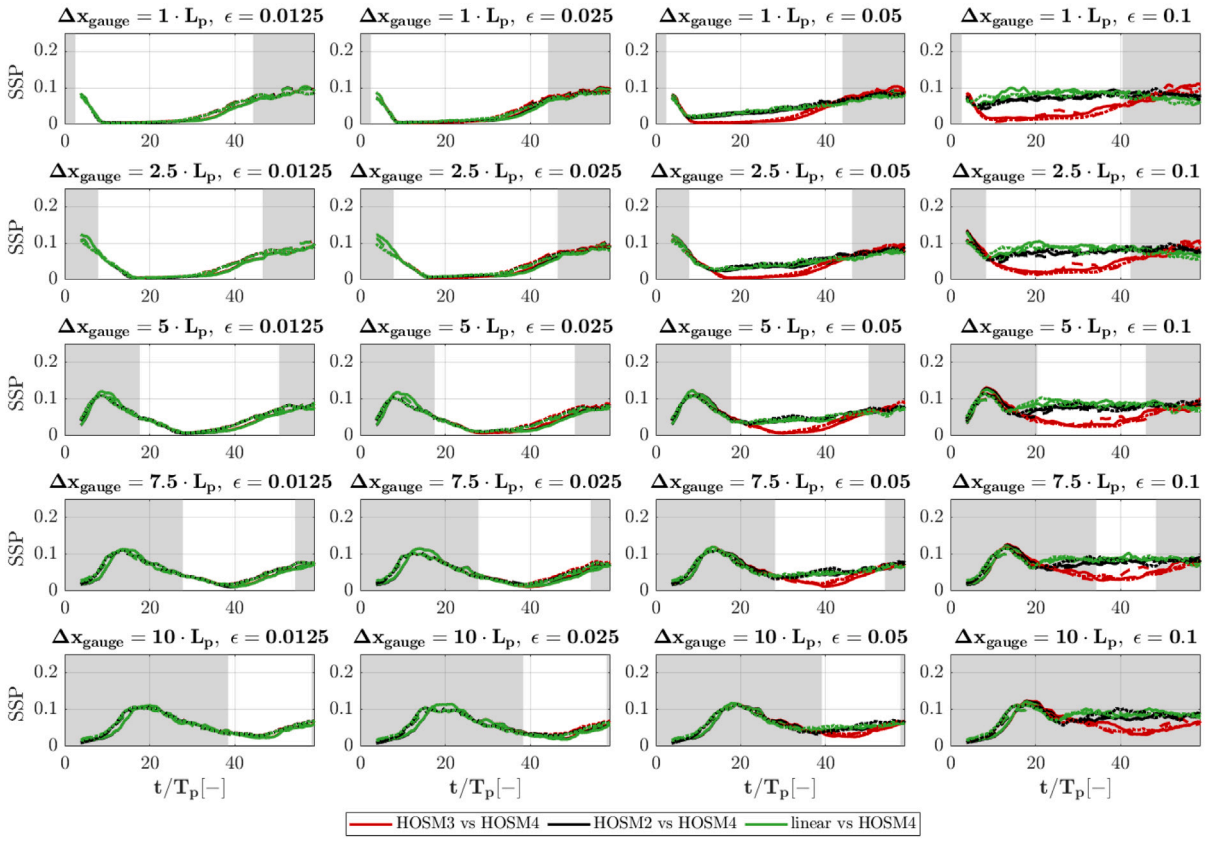

Fig. 11. Standard deviation of the 100 random realizations per sea state for all evaluated sea states (Table 1) for $\gamma = 1$. The wave steepness is kept constant vertically and increases from left to right. Horizontally, the prediction distance (see the gauge locations in Fig. 2) is kept constant and increases from top to bottom.

determined by shifting one time series relative to the other (cf. Fig. 3) ensuring that a pure phase shift due to different underlying dispersion models was at least compensated on an average level. Fig. 10 presents the mean time shift related to the minimum mean SSP of linear vs HOSM4 (green), HOSM2 vs HOSM4 (black), HOSM3 vs HOSM4 (red) and HOSM4 vs HOSM4 (blue) for all sea states ($\gamma = 1$; Fig. 14 for $\gamma = 6$) and gauge positions. The solid curves represent deep water conditions, the dashed curves $d = 40\,\mathrm{m}$ and the dotted curves $d = 30\,\mathrm{m}$. The gray zones mark the areas where the SSP ≤ 0.1 threshold was not reached (in deep water) to keep the discussion on the relevant part of the diagrams. The time shift to identify the minimal SSP was applied on the wave sequence (prediction), and a positive time shift denotes that the matching wave sequence (prediction) arrived later at the wave gauge position.

For the smallest investigated wave steepness, no relevant time shift was determined which would lead to a better SSP. With increasing wave steepness, a relevant time shift is identifiable, increasing with steepness and following a fairly linear progression over time.

In the context of the variation of the water depth, it is noticeable that the time shift increases with decreasing water depth compared to the deep water case. Particularly noteworthy hereby is that HOSM3 vs HOSM4 and even HOSM4 vs HOSM4 show some time shift in intermediate water depth for the case with the steepest waves (HOSM4 performs only slightly better), whereas there is no relevant time shift for the same sea states in deep water condition. This observation indicates that the time shift may be related to the interaction between the cut-out wave sequence and the decreasing water depth not being directly related to the model order. Investigations in the Fourier space on the temporal change of the energy spectra of the wave sequence in the different water depths showed that numerical artifacts at very low frequencies emerged in the HOSM3 and HOSM4 simulations for the intermediate water depths. The investigation revealed that there is a correlation between the magnitude of the artifact, the wave steepness and the intermediate water depth, i.e. no artifact for deep water and increasing magnitude with increasing wave steepness and decreasing water depth (exclusively for the cut-out wave sequences).

4.7. Standard deviation of the prediction accuracy

The standard deviation of the prediction accuracy is discussed in the following. As mentioned in Section 3.4, 100 simulations with random initializations were performed for each state combination and water depth before calculating the respective mean value of the error indicator. Fig. 11 presents the standard deviation of the mean SSP presented in Fig. 6 (consecutive time windows of 60 s and 100 random realizations) for linear vs HOSM4 (green), HOSM2 vs HOSM4 (black) and HOSM3 vs HOSM4 (red) for all sea states ($\gamma = 1$; Fig. 15 for $\gamma = 6$) and gauge positions. The solid curves represent deep water conditions, the dashed curves $d = 40\,\mathrm{m}$ and the dotted curves $d = 30\,\mathrm{m}$. The gray zones again mark the areas where the SSP ≤ 0.1 threshold was not reached (in deep water) to keep the discussion on the relevant part of the diagrams.

Analyzing the diagrams in detail reveals that the standard deviation for all models is very small for the two smaller wave steepness cases over all distances and water depths — a distinct difference for the different water depths is not identifiable. With increasing steepness, a similar picture emerges as with the other diagrams shown before — the lower-order models perform worse, resulting in an increased standard deviation, while the standard deviation for HOSM3 remains low even for the steeper sea courses (especially up to the distance $\Delta x = 5 \cdot L_p$.

This denotes that HOSM3 not only provides a better mean SSP for the steeper cases of the investigated sea states and water depths, but also that the variance of individual predictions is significantly smaller and therefore more reliable from an application point of view.

4.8. Limitations of the proposed study

The limitations of the results presented are summarized in this section. First, only unidirectional irregular sea states were considered, leaving the influence of the directionality to a later stage of investigation. While the linear behavior of unidirectional wave fields can be directly extrapolated to directional waves, including the background processes defining the boundaries of the linear predictable area (Qi et al., 2018b), it is well known that the sea-state directionality impacts the relevance of the modeled non-linear effects. For instance, the recent study of Kim and Ducrozet (2024) shows that, even if good predictions of non-linear unidirectional wave fields can be obtained by taking into account the Stokes drift only (coming from self interactions), the inclusion of second-order interactions between waves of different frequencies becomes more impactful in the case of directional wave fields. On the other hand, due to their much lower computational cost in numerical simulations as well as simpler setups in experiments, unidirectional wave fields benefit from being a very useful approximation of the full picture of the problem. Balancing between the requirements in terms of computational effort and the gain of knowledge, our study is limited to unidirectional waves, although the proposed protocol is directly extendable to directional wave fields.

In addition, no effect of current has been considered. Because the space and time variability of currents is highly dependent on local conditions (e.g. local wind, bathymetry, tide), no standard setup of variable current could easily be incorporated into the parameters' space that aims at describing the problem of wave prediction in a generic way. Considering a current U that remains constant (i.e. steady and uniform) over the considered simulation domain and time implies a correction of the waves' angular frequency according to $\Omega_n = \omega_n + k_n U$. The corresponding phase and group velocities are then $c_n = \Omega_n/k_n = \omega_n/k_n + U$ and $c_{g_n} = \partial\Omega_n/\partial k_n = \partial\omega_n/\partial k_n + U$, which consists in adding a constant U to the velocities of every wave component n. This results in a linear shift of the boundaries of the predictable area in space by an amount Ut, and in time by an amount x/U, which can be calculated without performing simulations. Based on these elements, the current is disregarded in the present study and left aside for future investigations.

Last, this study assumed a perfect reconstruction of the input snapshot as a basis for the wave prediction. In real world applications, the reconstructed input snapshot based on radar measurements will deviate from the actual sea state. The inaccurate starting point of the wave prediction will result in an increasing error influencing the predictable area (Klein et al., 2020).

5. Conclusion and outlook

In this study, the influence of the modeling order on the predictable area of unidirectional non-linear waves was investigated. A numerical setup based on the propagation of surface spatial sections leading to predicted time series of surface elevation at five different positions was used. Wave models of different non-linearity were applied and compared to a fourth-order HOSM reference solution. The characteristic wave steepness of the wave field was varied, as well as the prediction distance, the water depth and the peak enhancement factor of the wave spectrum. A threshold on prediction accuracy (i.e. SSP $\leq$ 0.1) was chosen to define the predictable area.

The presented results are a good indicator on which modeling order is accurate enough for wave prediction, depending on the wave steepness and prediction distance. The linear wave model performed as expected; for the two smallest wave steepness, the accuracy is adequate, similar to the non-linear models. With increasing steepness and prediction distance, more complex models need to be applied to achieve sufficient accuracy and predictable area, respectively. HOSM2 showed good accuracy compared to HOSM4 for lower wave steepness up to $\epsilon = 0.025$ performing slightly better than linear theory. For steeper waves, the accuracy decreased strongly, and no accurate prediction was possible any more. The predictions with HOSM3 were almost identical to those with HOSM4 for all configurations. This results from the fact that third-order wave models already include four-wave interaction processes, which comprise the predominant energy transfers governing the non-linear dynamics of ocean waves. In addition, the results highlighted the strong influence of the peak enhancement factor γ, for which significantly better results can be obtained with higher γ values. Furthermore, it was shown that the extension of the section with the NewWave for simulations with HOSM is not worth the computational effort, particularly with a focus on 2D simulations where the application of the NewWave smoothing is undefined. The investigation on the identification of the limiting wave groups defining the predicable area revealed that the predictable area depends on the prediction distance and decreases with increasing distance. This shows that the traditional method for the determination of the accessible prediction zone leads to conservative results, underestimating the predictable area (on the premise that an adequate wave model was chosen).

In general, it can be concluded that the order of non-linearity plays a pivotal role for accurate wave prediction to be adapted depending on the characteristic sea state conditions, e.g. accurate wave prediction is possible for a wide range of wave steepness and large prediction distance by suitable choice of the wave model.

As mentioned in the previous Section, the wave field directionality represents a straightforward choice of parameter that could be included in future studies on the topic. In addition, the impact of the reconstruction accuracy of the initial wave snapshot on the wave prediction and predictable area, respectively, would be of significant interest.

Funding

This paper is published as a contribution to the joint research project EproBOSS. The authors wish to express their gratitude to the German Federal Ministry for Economic Affairs and Climate Action (BMWK) and Project Management Jülich (PtJ) for funding and supporting the project (M.K. and N.H., grant number 03SX510A).

CRediT authorship contribution statement

Marco Klein: Writing – review & editing, Visualization, Supervision, Software, Resources, Project administration, Methodology, Funding acquisition, Conceptualization. **Helene Lünser:** Writing – original draft, Visualization, Validation, Software, Methodology, Investigation, Formal analysis, Data curation. **Moritz Hartmann:** Writing – review & editing, Validation, Software. **Sören Ehlers:** Writing – review & editing, Funding acquisition, Conceptualization. **Norbert Hoffmann:** Writing – review & editing, Supervision, Funding acquisition, Conceptualization. **Nicolas Desmars:** Writing – review & editing, Validation, Software, Methodology.

Declaration of competing interest

The authors declare that they have no known competing financial interests or personal relationships that could have appeared to influence the work reported in this paper.

Appendix. Results for $\gamma = 6$

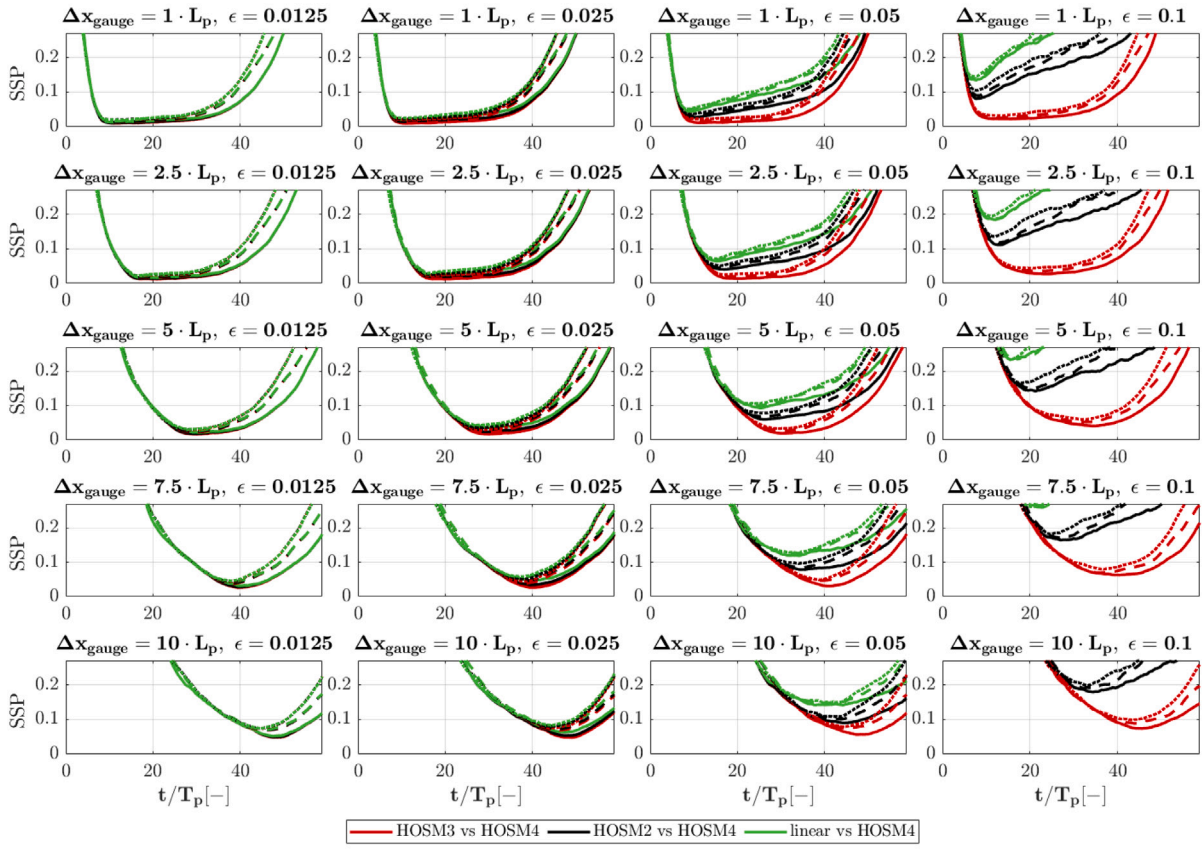

Fig. 12. SSP for all evaluated sea states (Table 1) with $\gamma = 6$. The wave steepness is kept constant vertically and increases from left to right. Horizontally, the prediction distance (see the gauge locations in Fig. 2) is kept constant and increases from top to bottom.

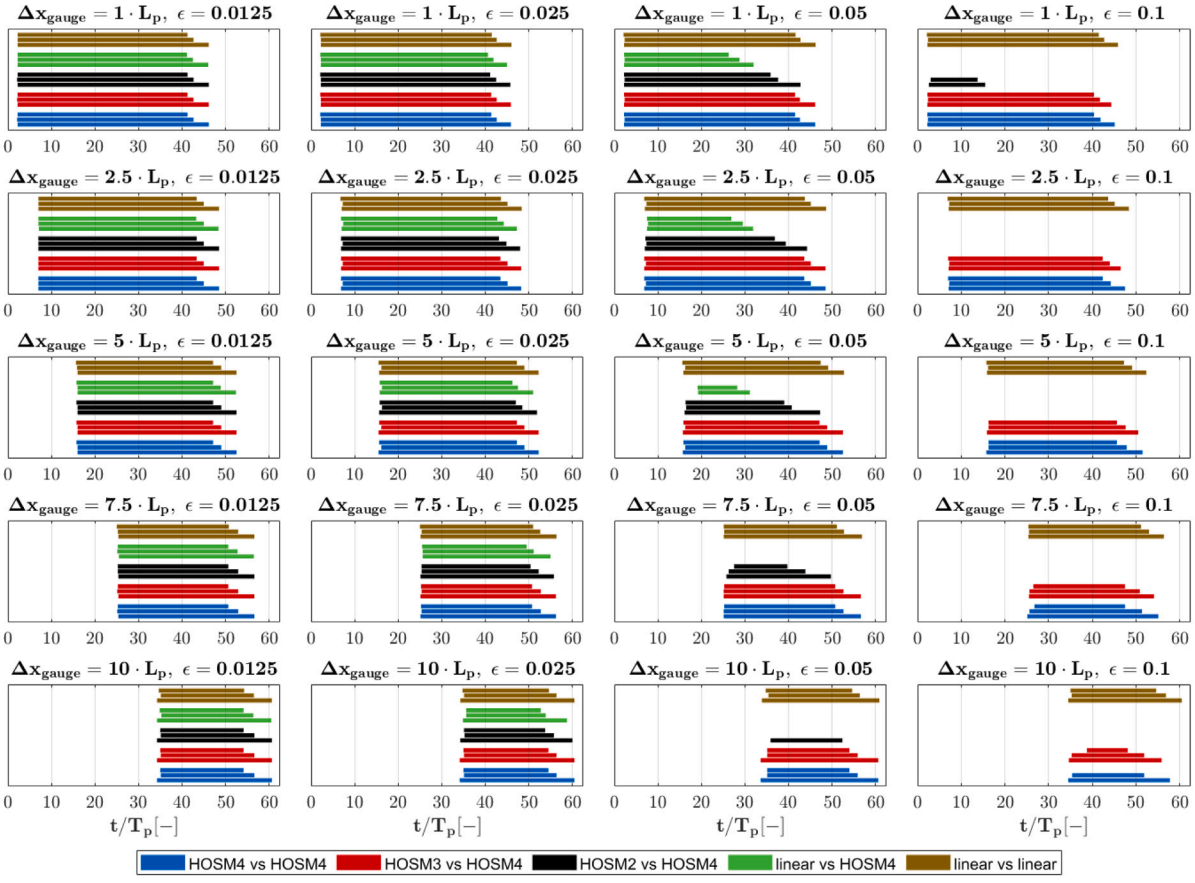

Fig. 13. Predictable area for all investigated sea states with $\gamma = 6$.

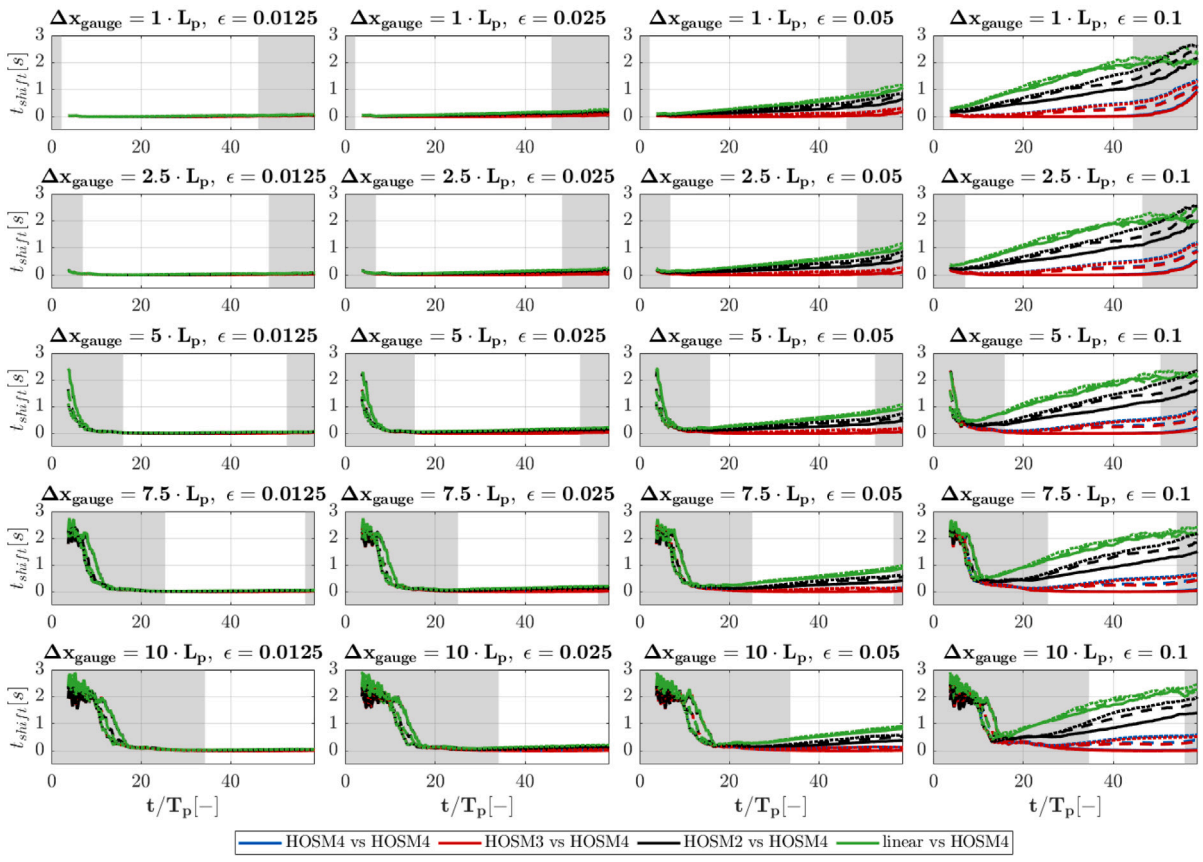

Fig. 14. Optimal time shift for all evaluated sea states (Table 1) for $\gamma = 6$. The wave steepness is kept constant vertically and increases from left to right. Horizontally, the prediction distance (see the gauge locations in Fig. 2) is kept constant and increases from top to bottom.

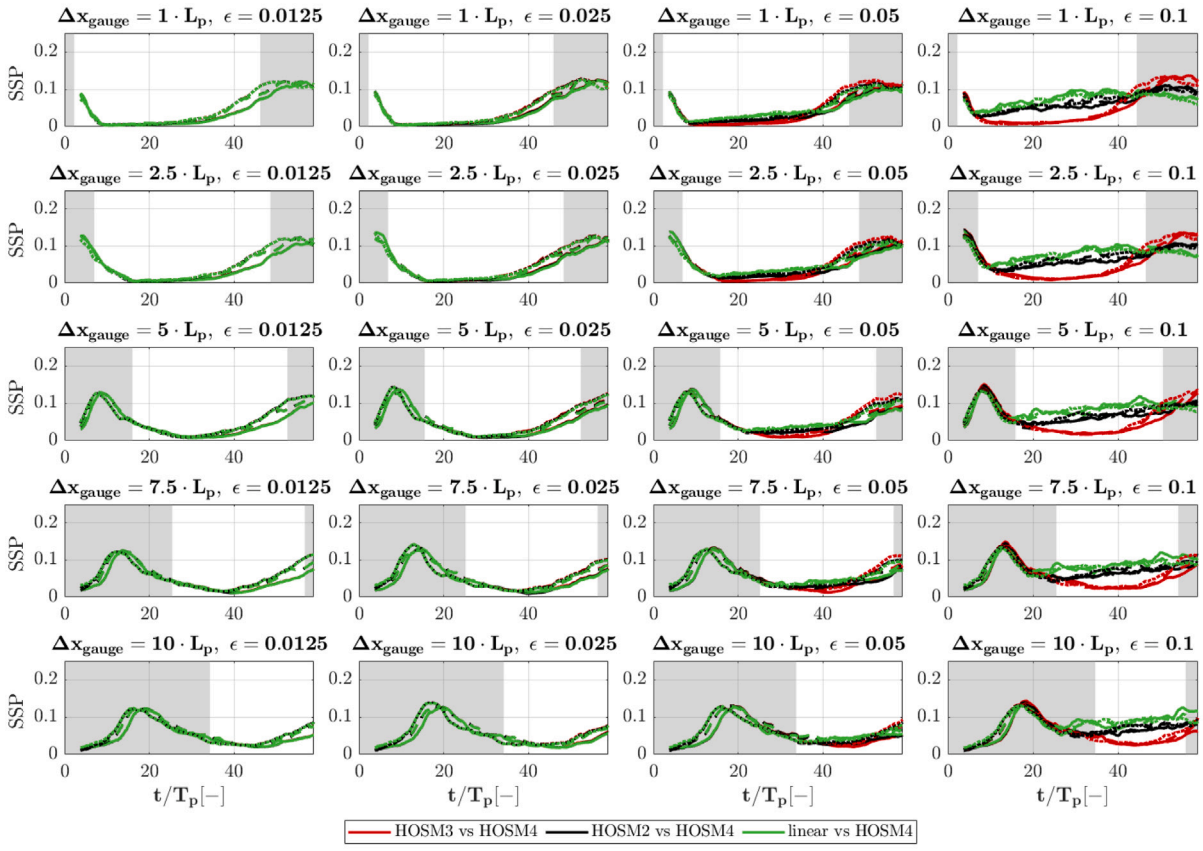

Fig. 15. Standard deviation of the 100 random realizations per sea state for all evaluated sea states (Table 1) for $\gamma = 6$. The wave steepness is kept constant vertically and increases from left to right. Horizontally, the prediction distance (see the gauge locations in Fig. 2) is kept constant and increases from top to bottom.

References

Airy, G., 1845. Tides and waves. Encycl. Metrop. 241–396.

Benjamin, T.B., Feir, J.E., 1967. The disintegration of wave trains on deep water part 1. Theory. J. Fluid Mech. 27 (3), 417–430. http://dx.doi.org/10.1017/S002211206700045X.

Blondel, E., Bonnefoy, F., Ferrant, P., 2010. Deterministic non-linear wave prediction using probe data. Ocean Eng. 37 (10), 913–926. http://dx.doi.org/10.1016/j.oceaneng.2010.03.002, URL http://www.sciencedirect.com/science/article/pii/S0029801810000661.

Bouws, E., Günther, H., Rosenthal, W., Vincent, C.L., 1985. Similarity of the wind wave spectrum in finite depth water: 1. spectral form. 90 (C1), 975–986. http://dx.doi.org/10.1029/JC090iC01p00975.

Clauss, G.F., Kosleck, S., Testa, D., 2012. Critical situation of vessel operations in short crested seas - forecast and decision support system. ASME J. Offshore Mech. Arct. Eng. 134(3):031601, 387–400. http://dx.doi.org/10.1115/1.4004515.

Clauss, G., Kosleck, S., Testa, D., Stück, R., 2007. Forecast of critical wave groups from surface elevation snapshots. In: OMAE 2007 - 26th Conference on Offshore Mechanics and Arctic Engineering. San Diego, USA.

Desmars, N., Hartmann, M., Behrendt, J., Hoffmann, N., Klein, M., 2023. Nonlinear deterministic reconstruction and prediction of remotely measured ocean surface waves. J. Fluid Mech. 975, A8. http://dx.doi.org/10.1017/jfm.2023.841.

DNV-RP-C205, 2023. Environmental conditions and environmental loads. DNV Recomm. Pr..

Dommermuth, D., 2000. The initialization of nonlinear waves using an adjustment scheme. Wave Motion 32 (4), 307–317. http://dx.doi.org/10.1016/S0165-2125(00)00047-0, URL http://www.sciencedirect.com/science/article/pii/S0165212500000470.

Dommermuth, D.G., Yue, D.K., 1987. A high-order spectral method for the study of nonlinear gravity waves. J. Fluid Mech. http://dx.doi.org/10.1017/S002211208700288X.

Fujimoto, W., Waseda, T., Webb, A., 2019. Impact of the four-wave quasi-resonance on freak wave shapes in the ocean. Ocean. Dyn. 69 (1), 101–121. http://dx.doi.org/10.1007/s10236-018-1234-9.

Hasselmann, K., 1962. On the non-linear energy transfer in a gravity-wave spectrum part 1. general theory. J. Fluid Mech. 12 (4), 481–500. http://dx.doi.org/10.1017/S0022112062000373.

Hasselmann, K., Barnett, T., Bouws, E., Carlson, H., Cartwright, D., Enke, K., Ewing, J., Gienapp, H., Hasselmann, D., Kruseman, P., Meerburg, A., Müller, P., Olbers, D., Richter, K., Sell, W., 1973. Measurements of Wind-Wave Growth and Swell Decay During the Joint North Sea Wave Project (JONSWAP). Ergänzungsheft zur Deutschen Hydrographischen Zeitschrift A8(12), Deutsches Hydrographisches Institut, Hamburg.

Hlophe, T., Wolgamot, H., Kurniawan, A., Taylor, P.H., Orszaghova, J., Draper, S., 2021. Fast wave-by-wave prediction of weakly nonlinear unidirectional wave fields. Appl. Ocean Res. 112 (April), 102695. http://dx.doi.org/10.1016/j.apor.2021.102695.

Huchet, M., Babarit, A., Ducrozet, G., Ferrant, P., Gilloteaux, J.C., Droniou, E., 2023. Experimental assessment of a nonlinear, deterministic sea wave prediction method using instantaneous velocity profiles. Ocean Eng. 281, 114739. http://dx.doi.org/10.1016/j.oceaneng.2023.114739, URL https://www.sciencedirect.com/science/article/pii/S002980182301123X.

Janssen, P., 2004. The Interaction of Ocean Waves and Wind. Cambridge University Press.

Kim, I.C., Ducrozet, G., 2024. Real-time phase-resolved ocean wave prediction in directional wave fields: Second-order Lagrangian wave models. Ocean Eng. 313, 119316. http://dx.doi.org/10.1016/j.oceaneng.2024.119316, URL https://www.sciencedirect.com/science/article/pii/S0029801824026544.

Klein, M., Dudek, M., Clauss, G.F., Ehlers, S., Behrendt, J., Hoffmann, N., Onorato, M., 2020. On the deterministic prediction of water waves. Fluids 5 (1), 9. http://dx.doi.org/10.3390/fluids5010009.

Kosleck, S., 2013. Prediction of Wave-Structure Interaction by Advanced Wave Field Forecast (Ph.D. thesis). Dissertation, Technische Universität Berlin (D83).

Lünser, H., Hartmann, M., Desmars, N., Behrendt, J., Hoffmann, N., Klein, M., 2022. The influence of characteristic sea state parameters on the accuracy of irregular wave field simulations of different complexity. Fluids 7 (7), http://dx.doi.org/10.3390/fluids7070243, URL https://www.mdpi.com/2311-5521/7/7/243.

Mei, C.C., Stiassnie, M., Yue, D.K.P., 2005. Theory and Applications of Ocean Surface Waves. World Scientific, http://dx.doi.org/10.1142/5566.

Meisner, E., Galvagno, M., Andrade, D., Liberzon, D., Stuhlmeier, R., 2023. Wave-by-wave forecasts in directional seas using nonlinear dispersion corrections. Phys. Fluids 35 (6), http://dx.doi.org/10.1063/5.0149980, 062104.

Naaijen, P., van Dijk, R., Huijsmans, R., El-Mouhandiz, A.A., 2009. Real time estimation of ship motions in short crested seas. In: OMAE 2009 - 28th Conference on Offshore Mechanics and Arctic Engineering. Honolulu, USA.

Naaijen, P., Huijsmans, R., 2008. Real time wave forecasting for real time ship motion predictions. In: OMAE 2008 - 27th Conference on Offshore Mechanics and Arctic Engineering. Estoril, Portugal.

Naaijen, P., Huijsmans, R., 2010. Real time prediction of second order wave drift forces for wave force feed forward in DP. In: OMAE 2010 - 29th Conference on Offshore Mechanics and Arctic Engineering. Shanghai, China.

Naaijen, P., Trulsen, K., Blondel-Couprie, E., 2014. Limits to the extent of the spatio-temporal domain for deterministic wave prediction. Int. Shipbuild. Prog. 61 (3–4), 203–223. http://dx.doi.org/10.3233/ISP-140113.

Payer, H.G., Rathje, H., 2004. Shipboard routing assistance - decision making support for operation of container ships in heavy seas. In: SNAME Annual Meeting.

Perlin, M., Bustamante, M.D., 2016. A robust quantitative comparison criterion of two signals based on the Sobolev norm of their difference. J. Engrg. Math. http://dx.doi.org/10.1007/s10665-016-9849-7.

Qi, Y., Wu, G., Liu, Y., Kim, M.H., Yue, D.K.P., 2018a. Nonlinear phase-resolved reconstruction of irregular water waves. J. Fluid Mech. 838, 544–572. http://dx.doi.org/10.1017/jfm.2017.904.

Qi, Y., Wu, G., Liu, Y., Yue, D.K.P., 2018b. Predictable zone for phase-resolved reconstruction and forecast of irregular waves. Wave Motion 77, 195–213. http://dx.doi.org/10.1016/j.wavemoti.2017.12.001, URL http://www.sciencedirect.com/science/article/pii/S0165212517301518.

Simanesew, A., Trulsen, K., Krogstad, H.E., Borge, J.C.N., 2017. Surface wave predictions in weakly nonlinear directional seas. Appl. Ocean Res. 65, 79–89. http://dx.doi.org/10.1016/j.apor.2017.03.009, URL http://www.sciencedirect.com/science/article/pii/S0141118716303613.

Tromans, P.S., Anatruk, A.H., Hagemeijer, P., 1991. New model for the kinematics of large ocean waves application as a design wave. Proc. the First Int. Offshore Polar Eng. Conf. (January 1991), 64–71.

Trulsen, K., Stansberg, C.T., 2001. Spatial evolution of water surface waves: Numerical simulation and experiment of bichromatic waves. pp. ISOPE–I–01–247.

Wang, G., Zhang, J., Ma, Y., Zhang, Q., Li, Z., Pan, Y., 2022. Phase-resolved ocean wave forecast with simultaneous current estimation through data assimilation. J. Fluid Mech. 949, A31. http://dx.doi.org/10.1017/jfm.2022.765.

West, B.J., Brueckner, K.A., Janda, R.S., Milder, D.M., Milton, R.L., 1987. A new numerical method 'for surface hydrodynamics. J. Geophys. Research: Ocean. http://dx.doi.org/10.1029/JC092iC11p11803.

Wu, G., 2004. Direct simulation and deterministic prediction of large-scale nonlinear ocean wave-field (Ph.D. thesis). Massachusetts Institute of Technology. Dept. of Ocean Engineering.

Zakharov, V., 1968. Stability of period waves of finite amplitude on surface of a deep fluid.. J. Appl. Mech. Tech. Phys. 9 190–194.